PHYSICAL REVIEW B **85**, 235418 (2012)

Distinguishing carbon nanotube defect chemistry using scanning gate spectroscopy

Steven R. Hunt, Elliot J. Fuller, Brad L. Corso, and Philip G. Collins*

Department of Physics and Astronomy, University of California, Irvine, Irvine, California 92697 USA

(Received 25 April 2012; published 7 June 2012)

Electronic scattering at individual defect sites is presumably sensitive to defect chemistry. Here, we combine advances in carbon nanotube device fabrication and scanning probe characterization to investigate this correspondence. Specifically, we apply scanning gate spectroscopy (SGS) to the study of defects introduced into single walled carbon nanotubes by point functionalization in water, sulfuric acid, or hydrochloric acid. SGS measures the energy-dependent transmission functions of defect sites, and by working in the dilute limit of individual, isolated defects we empirically distinguish the three chemical types. A preliminary analysis proposes a scattering model in order to motivate further theoretical investigations of this one-dimensional scattering system.

DOI: 10.1103/PhysRevB.85.235418 PACS number(s): 73.63.Fg, 72.10.Fk, 85.35.Kt, 81.16.Pr

I. INTRODUCTION

Historically, optical spectroscopy has been the primary tool for characterizing point defects.[1,2] With the continued scaling of electronic devices, however, defect properties are now becoming directly accessible to electrical transport measurements. Various types of devices, including traditional Si field effect transistors (FETs), are now fabricated at scales for which the presence of a single atomic defect affects the device conductance, mobility, or fluctuations and noise.[3] Using high-purity devices made of Si, Ge, diamond, or compound semiconductors, a nascent field is growing around the concept of single atom electronics, sometimes termed "solotronics."[4,5]

Of the different low-dimensional conductors that are most sensitive to defects, the single walled carbon nanotube (SWNT) is an exceptional case. Pristine SWNTs are quasi-one-dimensional conductors with inelastic mean free paths that approach 1 μm at room temperature,[6–8] and these characteristics make their electronic properties unusually sensitive to individual defects.[9] The quasi-one-dimensionality of SWNT states means that every carrier propagating through the device is able to interact with the defect potential. The long mean-free path allows SWNT devices to be easily fabricated using conventional lithography, but still in a regime where other sources of inelastic scattering and dissipation are minimal. Besides these two advantages, the versatility afforded by carbon chemistry makes SWNTs a rich system where defect scattering sites can be chemically tailored to have many possible identities. Whereas traditional semiconductor defects are most likely to be atomic vacancies or interstitials, a SWNT defect site can incorporate an almost unlimited variety of covalently-bonded molecules,[10,11] and consequently, a range of scattering potentials. This versatility provides an opportunity for precisely mapping the correspondence between chemical structure and electronic function in the challenging limit of dilute disorder. Near-field optical techniques can locate individual defects, but not distinguish the properties of different chemical types.[12–14] Transport measurements, on the other hand, are sensitive to individual defects, especially in the quasi-ballistic limit where one defect is the primary source of resistance.[8,15,16] This sensitivity provides a possible experimental method for identifying and categorizing different types of defects.

In order to test this hypothesis and characterize SWNT defects electronically, we developed the electrochemical technique of point functionalization[15] to add individual point defects to operational SWNT FETs. By measuring the same SWNT before and after deliberate chemical modification, we can directly observe the change in electrical characteristics caused by the added disorder. To spatially resolve these effects and more precisely investigate the role of the defect sites, we combine the electrical measurements with simultaneous scanning probe interrogation.[17] An electrostatic potential V_{tip} on a conductive, scanning probe tip allows a SWNT to be locally gated, independently from the rest of the device. When performed using fixed biases, this scanning probe technique is known as scanning gate microscopy (SGM), and it creates a spatial image of the channel transconductance at particular bias conditions.[18–25] We have combined SGM with more traditional SWNT transport spectroscopy[7,8] by sweeping through multiple values of the backgate bias V_{bg}, source-drain bias V_{sd}, or V_{tip} at each position along a SWNT. This technique generates a multidimensional data set referred to as scanning gate *spectroscopy* (SGS). The SGS data provides a detailed record of the gate-dependent scattering that occurs in the immediate vicinity of a defect site.[26]

In this paper, we summarize the results of performing scanning gate spectroscopy on a variety of SWNT devices. A single defect has been analyzed in detail in a previous publication,[26] but here we describe the technique and apply it comparatively to SWNTs oxidized to different degrees in water or acids. Having oxidized multiple devices in each electrolyte, we demonstrate typical scattering characteristics for particular types of chemical modification. However, we also identify experimental variability that must be controlled before chemically distinct defects can be reliably categorized.

II. EXPERIMENTAL METHODS

A. SWNT synthesis and device fabrication

For this work, SWNT FET devices were manufactured on 4″ Si wafers using techniques common for the field, namely chemical vapor deposition (CVD) and conventional optical lithography. Numerous recipes are available for the CVD growth of dilute, high quality SWNTs on Si wafers. Our implementation used a monodisperse nanoparticle, $Fe_{30}Mo_{84}$,

 ©2012 American Physical Society

as the catalytic seed to initiate SWNT growth. The nanoparticle seed was initially synthesized, following previous reports, as a water-soluble, ligand-terminated, icosahedral FeMo keggin molecule.[27,28] Using an excess of the metallorganic molecules in ethanol, a saturated solution was prepared at room temperature, allowed to settle, and then decanted. A 1000:1 dilution of the saturated solution was spun onto 4″ p^{++} Si wafers to produce a dilute but uniform coating. Oxidation in air at 700 °C collapses the keggin molecules into catalytically active, solid particles that are suitable for growing dilute, isolated SWNTs at an areal density of approximately 0.1 μm^{-2}.[28,29]

SWNT synthesis occurred in a custom-built, 115 mm quartz tube furnace operating at 940 °C. After an initial reduction of the particles in H_2 (520 sccm) and Ar (3000 sccm), the addition of CH_4 (1000 sccm) initiates the spontaneous nucleation and growth of SWNTs. Similar conditions in smaller furnaces have been reported to grow SWNTs with long lengths and excellent electrical characteristics.[28,29] Our SWNTs are characterized by a combination of scanning electron microscopy (SEM, Philips XL-30 at 1 kV) and by noncontact atomic force microscopy (AFM) (Pacific Nanotechnology Nano-R). SWNTs in this report fall in a diameter range of 1.1–1.7 nm, with process variations such as residual H_2O contributing to smaller or larger SWNTs.

After CVD, wafers were processed with optical lithography to define Ti or Ti/Pt electrodes on top of the randomly grown SWNTs. An undercut bilayer resist (S1808 on top of LOR-A1, MicroChem) was used to improve liftoff and give cleaner interfaces. The separation between source and drain electrodes was typically 2 μm, though SWNTs oriented at an angle to the electrodes produced longer channel lengths. The p^{++} substrate, separated from the SWNTs by a 250 nm SiO_2 thermal oxide, provided a shared back-gate electrode. Automated, wafer-scale electrical characterization identified individual SWNT devices to be either semiconducting or metallic, in approximately the 2:1 ratio predicted theoretically.[30,31]

B. Defect incorporation by point functionalization

After initial characterization of a SWNT in its pristine state, selected devices were chemically modified to incorporate different types of defects. The general procedure, described previously as point functionalization,[15,32,33] involves driving an electrochemical oxidation reaction between the SWNT and an electrolyte while monitoring for changes in the SWNT conductance G. After the initial electrochemical charging of double layer capacitances, the covalent addition of individual defects is revealed by discrete changes in $G(t)$.[15,32,33] This report focuses on defects produced using oxidation in DI water (18 MΩ, Nanopure), concentrated sulfuric acid (18 M H_2SO_4), or concentrated hydrochloric acid (12 M HCl). Evidence exists for associating H_2O oxidation with −OH adducts, H_2SO_4 oxidation with ethers and epoxides, and HCl oxidation with −Cl adducts. Nevertheless, the exact chemical nature is not the focus of this report, so the results and discussion simply name the defects according to the starting electrolyte.

To introduce defects, a device was first coated in poly(methyl methacrylate) (PMMA A3, MicroChem) and patterned to expose a 0.5–1.0 μm long portion of the SWNT channel. This exposure window was centered at the device midpoint to spatially separate the results of point functionalization from features like Schottky barriers at either end of the SWNT channel. AFM imaging confirmed the positioning of the exposure window over each SWNT and the presence of a protective coating over the remaining majority of the surface, including the source and drain electrodes and the electrode-SWNT interfaces. Using an *xyz* manipulator, microtubing (0.030″) containing electrolyte was positioned over the exposed region and lowered to bring a small droplet into contact with the surface. The electrolyte potential was controlled using a Pt pseudo-reference electrode located in the droplet at the chip surface. Electrochemical modifications were controlled using a custom-built, multipotential bipotentiostat and LABVIEW software. The SWNT source, drain, and gate electrodes as well as an additional Pt counter electrode, were all independently controlled with respect to the Pt pseudoreference during electrochemical modifications. In this scheme, the exposed portion of SWNT constitutes an electrochemical working electrode, and oxidation of the SWNT was performed by biasing it at 0.9 to 1.2 V (versus Pt), depending on the oxidative threshold of each electrolyte used.[15] Simultaneously, the SWNT conductance G was independently monitored by applying a source-drain potential $V_{sd} = 0.1$ V and digitizing a transimpedance current preamplifier (Keithley 428) at 100 kHz. After oxidation had reduced G below a selected threshold, each SWNT is electrochemically reduced to drive off noncovalently bound counter ions and recover a portion of the initial value.

After chemical modification, an acetone soak was used to strip the protective PMMA and expose the entire device for further AFM imaging. Stable electrical behavior indicated that the PMMA removal did not affect the chemistry of the SWNT modifications. We note that a much simpler process is to perform point functionalization without any PMMA processing; but in this case, the technique preferentially creates defects within 500 nm of an electrode, which compromises subsequent scanning probe imaging.

C. Electrical characterization and scanning gate spectroscopy

Three-terminal FET characteristics were measured using dc and ac techniques over a temperature range of 77–300 K. Point functionalized devices always exhibited a lowered conductance $G(V_{bg}, V_{sd})$ at some backgate voltages V_{bg}, and this decrease grew stronger at lower temperatures. Comparing $G(V_{bg}, V_{sd})$ characteristics before and after chemical modification indirectly measured the electronic consequences of the added defects.

To spatially resolve these effects and more precisely investigate defect scattering, we acquired SGM images of $G[V_{bg}, V_{sd}, V_{tip}(x,y)]$ by probing the SWNT with a conductive, scanning probe. In this technique, the additional dc potential V_{tip} on a probe tip allows small portions of a SWNT to be electrostatically gated independently from the rest of the device. The resulting SGM image is a real space representation of the modulation ΔG that occurs for selected biases,[17] and it has been established as a useful technique for identifying defects.[15,19–22,34]

Figure 1(a) shows an example SGM image for a semiconducting SWNT (s-SWNT) device, with the measurement

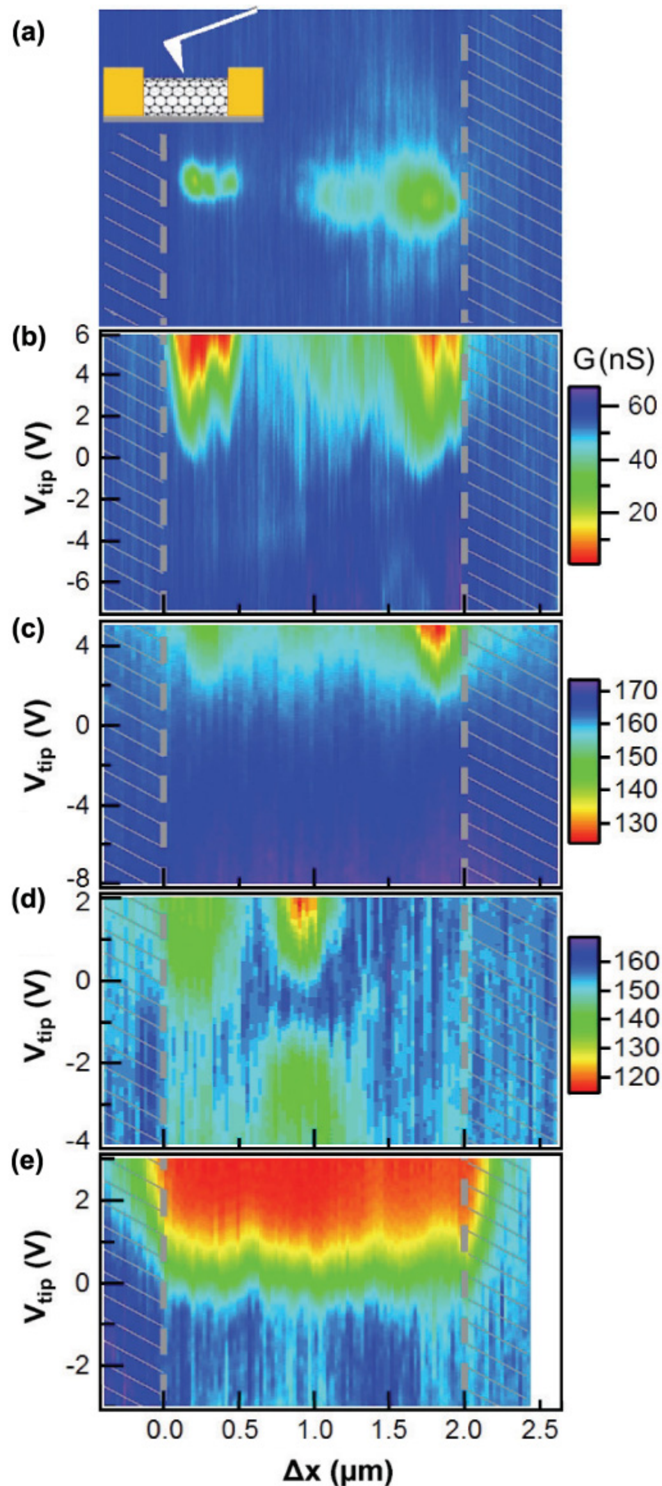

FIG. 1. (Color online) (a) SGM and (b) corresponding SGS image of an s-SWNT having Schottky barriers at both electrodes and an additional, weakly scattering defect in the channel at $\Delta x = 1.2\ \mu$m. Approximate position of source and drain electrodes are indicated with grey striping. Inset depicts the measurement geometry. (c) SGS for a similar s-SWNT over a different range of V_{tip}. (d) SGS image for a strongly scattering defect in a SWNT with only one sensitive interface. (e) SGS image for a pristine, small-bandgap SWNT that exhibits no appreciable Schottky barriers.

geometry indicated in the inset. Dashed lines indicate the extent of the source and drain electrodes, over which V_{tip} has no effect on G and the image is uniform. Along the s-SWNT channel, the most prominent features correspond to Schottky barriers where the SWNT meets the source and drain electrodes. A weaker, circularly symmetric feature near the middle of the image is the result of point functionalization. The image illustrates how SGM can confirm the presence of this added disorder, but the technique is clearly not sufficient to characterize the site quantitatively.

The scanning gate spectroscopy (SGS)[26] technique improves upon SGM by sweeping through multiple values of V_{bg}, V_{sd}, or V_{tip} at selected tip positions, in order to study the scattering at such a site. In our implementation, SGS mapping was accomplished using a high vacuum AFM system (JEOL JSPM-5200) with a liquid nitrogen cooled sample mount. AC conductance was measured using a standard lock-in technique simultaneously with topography,[35–38] using dual multifunctional data acquisition boards (National Instruments NI-6289) controlling the applied biases and the tip motion. The system, controlled by LABVIEW software, allowed the AFM tip to be paused over predefined positions on the topographic image, in order to sweep V_{bg} or V_{tip} along the SWNT rather than at every pixel on the surface. Unless noted otherwise, all SGM and SGS images are acquired at a temperature of 130 K and pressure $<5 \times 10^{-7}$ Torr. Compared to ambient, these conditions greatly reduce noise and minimize hysteresis from mobile surface contaminants.[22,39]

As a multidimensional surface map, a SGS data set is more difficult to represent than a SGM image. In this report, all SGS data is represented by two-dimensional color plots of $G(\Delta x, V_{tip})$. The spatial coordinate Δx in all of the images presented here corresponds to a line of pixels selected along the SWNT from source to drain electrode, while the second axis depicts the V_{tip} dependence. Figure 1(b) provides an example SGS image for the same device as Fig. 1(a), illustrating the alignment of features along the spatial axis and the disappearance of features at progressively negative V_{tip} values. The SGS information content along the V_{tip} axis is the main focus of the results and discussion.

III. RESULTS AND DISCUSSION

This report is primarily concerned with the SGS characterization of defects. The interpretation of SGS images is the focus of Secs. III A and III B, with particular attention paid to the SWNT-to-SWNT variations that complicate direct comparisons among devices. Secs. III C and III D summarize the SGS differences that we attribute to defect chemistry, as achieved by point functionalizing multiple devices in each of the three electrolytes studied. Finally, Sec. III E addresses the consequences of unintended variations in the point functionalization technique.

A. Imaging of single defect sites

Even among straight, clean SWNTs of a particular class (metallic or semiconducting), significant differences arise in SGS data sets. Figure 1 depicts SGS images acquired on four s-SWNT devices, demonstrating some of this sample

variability among s-SWNTs. In Fig. 1(b), a weakly scattering defect centered at $\Delta x = 1.2\ \mu$m is visible midway between two Schottky barriers. A second, nearly identical s-SWNT device has a weak feature at $\Delta x = 0.9\ \mu$m [see Fig. 1(c)]. A third s-SWNT exhibits much stronger contrast at its defect site [see Fig. 1(d)]. A comparison of the G and total modulation ΔG in each device shows that these parameters cannot be primarily responsible for the difference in defect contrast.

The main difference between these three examples is not the defect site *per se*, but the relative sensitivity of the Schottky barrier in each. In s-SWNTs, the electronic band gap is inversely proportional to diameter, and a lack of strong pinning by midgap states allows the Schottky barrier to vary freely from one device to another.[37,40] Even when fabricated with the same contact metal, devices having slightly different SWNT diameters exhibit a range of Schottky barrier heights.[38,41,42] SWNT diameters of 1.0–1.3 nm have large Schottky barriers that dominate $G(V_{bg})$ characteristics and minimize the relative contribution from defects [see Figs. 1(b) and 1(c)]. SWNTs with larger diameters of 1.4–1.7 nm have smaller barriers that allow defects to contribute more to the total resistance or, in this case, to the enhanced contrast observed in Fig. 1(d).

Still larger SWNTs have vanishingly small Schottky barriers that are not effectively gated by the SGM or SGS techniques. Figure 1(e) depicts a defect-free s-SWNT with a diameter of 2.0 nm, where Schottky barriers are not evident. Instead, the device has spatially uniform SGS modulation that is the hallmark of an intrinsic response of the SWNT band structure. Values of $V_{tip} > 1$ V locally deplete carriers and pinch off the channel equally well at any position along the SWNT. At $V_{tip} < -1$ V, the local accumulation of carriers does not enhance G, so that G becomes nearly insensitive to the probe tip position. At intermediate values $-1 < V_{tip} < 1$ V, the response shown in Fig. 1(e) is fairly uniform, with slight variations arising from contaminants and inhomogeneities in the underlying SiO_2.[43–45]

In our experience, defects added to large diameter s-SWNTs like the one in Fig. 1(e) have been difficult to study. The scattering added by a defect is only observed at V_{tip} values close to the band edge (i.e., $|V_{tip}| < 1$ V), where it is difficult to distinguish from substrate disorder. Furthermore, $G(V_{tip})$ data acquired directly over a defect site contains a mixture of contributions from both the defect and band structure depletion nearby. The minimal separation in V_{tip} between the band edge and a defect limits our ability to isolate the defect's energy-dependent contributions from other electrostatic effects.[46] By comparison, the spatially distinct features shown in Figs. 1(b)–1(d) provide much easier systems to analyze. Not only are the defects spatially separated from the Schottky barriers, but the band edges are fully outside the V_{tip} measurement range. In small-diameter SWNT devices like these, defect contrast occurs at V_{tip} values very close to the threshold for Schottky barriers and far from the band edges.

This empirical observation is an important point that merits emphasis. Each Schottky barrier or defect has a threshold V_{tip} value above which it begins to reduce G. In Fig. 1(b), for example, the left and right Schottky barriers have thresholds of 0 and -1 V, respectively. The threshold of the defect response is slightly higher, in the range of 1.5 to 2 V. In all three devices Figs. 1(b)–1(d) the defect threshold for sensitivity is found approximately 1.5 V higher than the Schottky barrier threshold. This similarity is reproduced in a wide range of small diameter, oxidized s-SWNTs. The observation suggests that the chemical potential of defect sites is pinned to a value set by the Schottky barrier threshold, at least in these cases where a strong Schottky barrier exists. This is very different from the case for larger diameter SWNTs, for which the Schottky barrier vanishes and defects are observed near the band edge. The interpretation of this difference is postponed to the next section, which first establishes V_{tip} as a proper energy scale.

Finally, we note that it is very typical for the source and drain Schottky barriers in a device to be unequal, as observed in Figs. 1(b)–1(d). V_{sd} does indeed break the symmetry of a device, but experiments reversing the bias prove that V_{sd} is only one component of the observed difference. Experience suggests that the greater causes are extrinsic. The SWNT-metal interface is poorly defined by liftoff processing, prone to contamination, and very difficult to precisely characterize. Thus we have been led to ignore differences in these barriers and have instead focused on point functionalization performed in the central region of the FET channel.

B. Electrostatic analysis of single defect sites

When a defect is located far from an electrode or other gate-dependent site, it appears in SGM as a symmetric, circular feature and in SGS as a quasi-parabolic curve. These two are equivalent, and the former shape has been clearly described in the literature.[19–22] The shape of features in an SGS image deserves special note, because the apparent defect size and explicit bias dependence in SGS images establishes the electrostatic coupling of the defect.

To model the effect of a defect on SGS imaging, we must consider both the geometry of this electrostatic coupling [see Fig. 2(a)] and the electronic structure of the defect itself. Due to evidence of Frenkel-Poole transport,[47,48] the defect is modeled as a localized state within a tunnel barrier that interrupts the SWNT band structure [see Fig. 2(b)]. The defect state itself extends around the SWNT circumference and some distance along the sidewall, but first-principles calculations predict various types of defects to have spatial extents of a few nm at most,[49–55] a scale ten times smaller than the lateral resolution of SGS. The defect state has a potential V_{defect} relative to the SWNT conduction band that is presumably sensitive to defect chemistry. In practice, however, this dependence is a constant offset that is secondary to the capacitive coupling of the defect to the back gate and probe tip. Movement of the probe tip and, more precisely, the charge Q_{tip} located at the tip apex cause V_{defect} to vary during SGS imaging. At fixed V_{bg}, the dependence is

$$V_{defect} = \frac{Q_{tip}}{4\pi\varepsilon_o r}, \tag{1}$$

where r is the distance from tip apex to the relevant SWNT segment, and ε_o is the dielectric constant in vacuum. By evaluating Q_{tip} in terms of the capacitance C_{tip-bg} between the tip and back gate,[56] and expressing r in terms of its vertical and horizontal components, we arrive at the practical

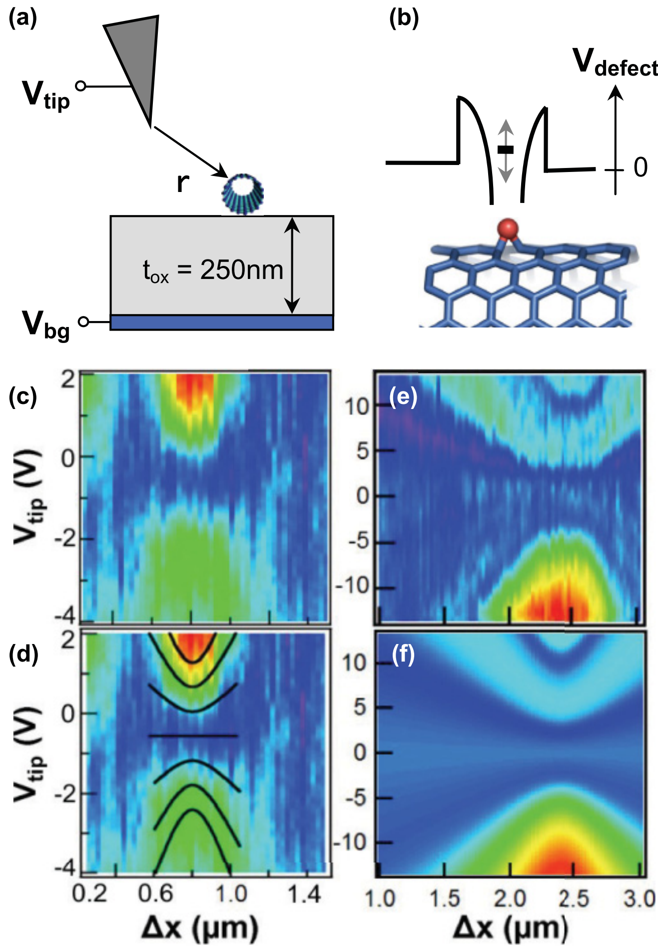

FIG. 2. (Color online) (a) Geometry defining the electrostatic coupling between a segment of the SWNT and $V_{\rm tip}$ and $V_{\rm bg}$. (b) Band diagram of a localized defect state interrupting the conduction band at the position of a defect. The potential of the state $V_{\rm defect}$ relative to $V_{\rm sd}$ is varied by the tip position and potential. The SWNT cartoon depicts an ether functionality believed to result from H_2SO_4 oxidation. (c) and (d) SGS profile of a defect with and without overlaid curves indicating fits to the contours of constant conductance. The voltage- and x-dependent contours determine the values of $C_{\rm tip-bg}$ and $V_{\rm defect}$, as described in the text. (e) and (f) An example of the agreement between experimental SGS data (e) and a simple electrostatic model (f) that correctly simulates the voltage and x dependencies.

expression

$$V_{\rm defect} = \frac{C_{\rm tip-bg}(V_{\rm tip} - V_{\rm bg})}{4\pi\varepsilon_o\sqrt{x^2+z^2}}. \quad (2)$$

Equation (2) predicts the specific dependence of $V_{\rm defect}$ solely in terms of experimentally-controlled variables x, z, $V_{\rm tip}$, and $V_{\rm bg}$, where x is the lateral distance to a defect site and z is the height of the probe tip above the oxide surface. The sole unknown term in Eq. (2) is the capacitance $C_{\rm tip-bg}$. This term has been extensively considered in the geometry of scanning probe tips because, for example, its value is necessary for the quantitative evaluation of SGM and other scanning probe images. Fortunately, $C_{\rm tip-bg}$ depends logarithmically on z, so it is very nearly constant in this experimental geometry.[56]

The raw SGM and SGS data measure conductance G as a function of the same variables found in Eq. (2). However, analytical conversion of the G data into $V_{\rm defect}$ values is intractable without *a priori* knowledge of the analytical form of G. Instead of assuming a particular expression, we use a purely geometric argument to interconvert between the two. Specifically, we assume G to be proportional to the defect's transmission T_d, an energy-dependent function, when the tip is near a defect.[57] Contours of constant G denote contours of constant $T_d(V_{\rm defect})$ and, if T_d is a smooth function of $V_{\rm defect}$, they can be interpreted as contours of constant $V_{\rm defect}$ without knowing the precise functional form of $G(V_{\rm defect})$.

Two aspects of the data in Fig. 1 illustrate this argument. First, contours of constant $V_{\rm defect}$ must form circles around a defect site in a conventional SGM image, as seen in Fig. 1(a). Second, the same contours must follow the curve of Eq. (2) in the Δx-$V_{\rm tip}$ plane of a SGS image. To highlight the agreement of the data with Eq. (2), Fig. 2(c) reproduces just the defect region from Fig. 1(d), and Fig. 2(d) shows an example set of contours overlaid on the data, with contours of constant G curving through the Δx-$V_{\rm tip}$ plane. Extracting multiple contours from the data and fitting them to Eq. (2) determines the capacitance $C_{\rm tip\text{-}bg}$ with no free parameters, allowing each contour to be assigned a definite $V_{\rm defect}$ value. The lines chosen in Fig. 2(d) are evenly spaced from $V_{\rm defect} = -0.3$ to $+0.3$ V at intervals of 0.1 V. The proportionality factor $V_{\rm defect}/V_{\rm tip}$ ranges from 0.08 to 0.22 for typical SGS operating conditions. Thus, by explicitly measuring $G(\Delta x, V_{\rm tip})$, the SGS technique achieves a significant result: a direct and calibrated conversion of the experimental bias $V_{\rm tip}$ into the local potential $V_{\rm defect}$ responsible for the added resistance, without assuming any particular model function for $T_d(V_{\rm defect})$.

This fitting process clarifies the size and shape of features in SGS images. When the probe tip is centered directly over a defect site, the $G(V_{\rm tip})$ response is extremal. Attenuated responses away from the defect determine the system capacitance and allow $V_{\rm tip}$ to be converted into $V_{\rm defect}$. Otherwise, the nonextremal $G(V_{\rm tip})$ values contain no new information about the defect's nature or scattering, and certainly do not reflect the physical size of the defect itself. In fact, the defect position and size are best determined by the residual errors obtained from fitting contours to Eq. (2). The feature in Fig. 2(c) appears 450 nm wide, but a single, simultaneous fit to the multiple contours in Fig. 2(d) determines the defect position to within 15 nm. Within this resolution limit, the defect is indistinguishable from a point scatterer.

The extremal $G(V_{\rm tip})$ response at the defect position fully describes a defect's transmission, at least for particular biases $V_{\rm sd}$ and $V_{\rm bg}$. To illustrate this point, Fig. 2(e) shows an SGS image with three distinct local maxima in $G(V_{\rm tip})$. Average $G(V_{\rm tip})$ values around $x = 2.4$ μm were extracted and used with Eq. (2) to simulate an SGS image in Fig. 2(f). The simulation and raw data agree very well, even though the particular shape of $G(V_{\rm tip})$ is complex. The example shows that the contours are wholly insensitive to defect identity and that, once $C_{\rm tip\text{-}bg}$ has been determined, a single curve of $G(V_{\rm defect})$ extracted at an extremal value is sufficient to describe the defect's electronic properties. This conclusion simplifies our comparisons in Sec. III C of defects having different chemistries.

Finally, application of the Landauer-Buttiker model[58] allows $G(V_{\text{defect}})$ to be converted into an energy-dependent transmission coefficient $T_d(V_{\text{defect}})$. In the strong scattering limit, the two are simply proportional, but the maximum value of T_d depends sensitively on the rest of the device. Before point functionalization, the SWNT and its Schottky barriers can be treated as a single, lumped element G_{pristine}. After point functionalization, G_{pristine} is in series with the defect contribution $G(V_{\text{defect}})$. By taking advantage of measurements performed on the same SWNT device before and after defect incorporation, we calculate T_d by separating out the G_{pristine} contribution,

$$T_d^{-1} = 1 + G_o\left(\frac{G_{\text{pristine}} - G}{G_{\text{pristine}}G}\right), \tag{3}$$

where $G_o = 4e^2/h$ for a SWNT. Unfortunately, relatively high Schottky barriers or other contact resistances in these devices give G_{pristine}/G_o values that are typically in the range of 0.5 to 5%. This low transmission by the contacts limits our ability to clearly resolve very small changes in T_d caused by the defect. At room temperature, for example, $(G_{\text{pristine}} - G)$ often approaches zero, so that the defect transmission is definitely higher than the contact transmission but not necessarily approaching unity. Fortunately, measurements at 130 K always show a substantial difference $(G_{\text{pristine}} - G)$, so that the maximum value of T_d is well defined by the SGS data considered here.

C. Comparison among electrolytes

Data for representative SWNT devices oxidized in H_2O, H_2SO_4, and HCl are shown in Fig. 3. For each electrolyte, the portion of an SGS image centered around a defect and an extremal $G(V_{\text{tip}})$ curve extracted from the image are both shown. On the right hand side of the image, a calculated $T_d(V_{\text{tip}})$ curve is shown. Using the capacitance $C_{\text{tip-bg}}$ derived from each image, V_{tip} is also converted into a local potential V_{defect}.

Figure 3(a) depicts the simplest possible type of defect barrier, and it is typical of that observed after point oxidation in H_2O. The SGS image shows a high-G channel for $-1 < V_{\text{tip}} < 0$ V, in which the defect transmission peaks at $V_{\text{defect}} = 0$. When gated away from this ideal value, the defect state is no longer resonant and G decreases. This particular data set was analyzed in detail previously[26] using the assumption that T_d approached unity, but a more realistic assessment of the maximum transmission is shown here. We interpret the asymmetry in V_{tip} to arise from the difference between an attractive and repulsive defect state. For $V_{\text{tip}} > 0$, V_{defect} lies above the conduction band and it is repulsive (to electron carriers). For $V_{\text{tip}} < 0$, V_{defect} becomes an attractive trap state that may contribute to tunneling inelastically. A modest oscillation in G on the attractive side suggests the presence of a second state below -4 V.

Figure 3(b) depicts a barrier resulting from oxidation of an m-SWNT in H_2SO_4. The barriers formed by H_2SO_4 or H_2O oxidation both have similar, high transmission at $V_{\text{defect}} = 0$, but otherwise the SGS images can be characterized by qualitatively distinct features. First, the $G(V_{\text{tip}})$ curve for an H_2SO_4 defect is much more asymmetric than the H_2O case,

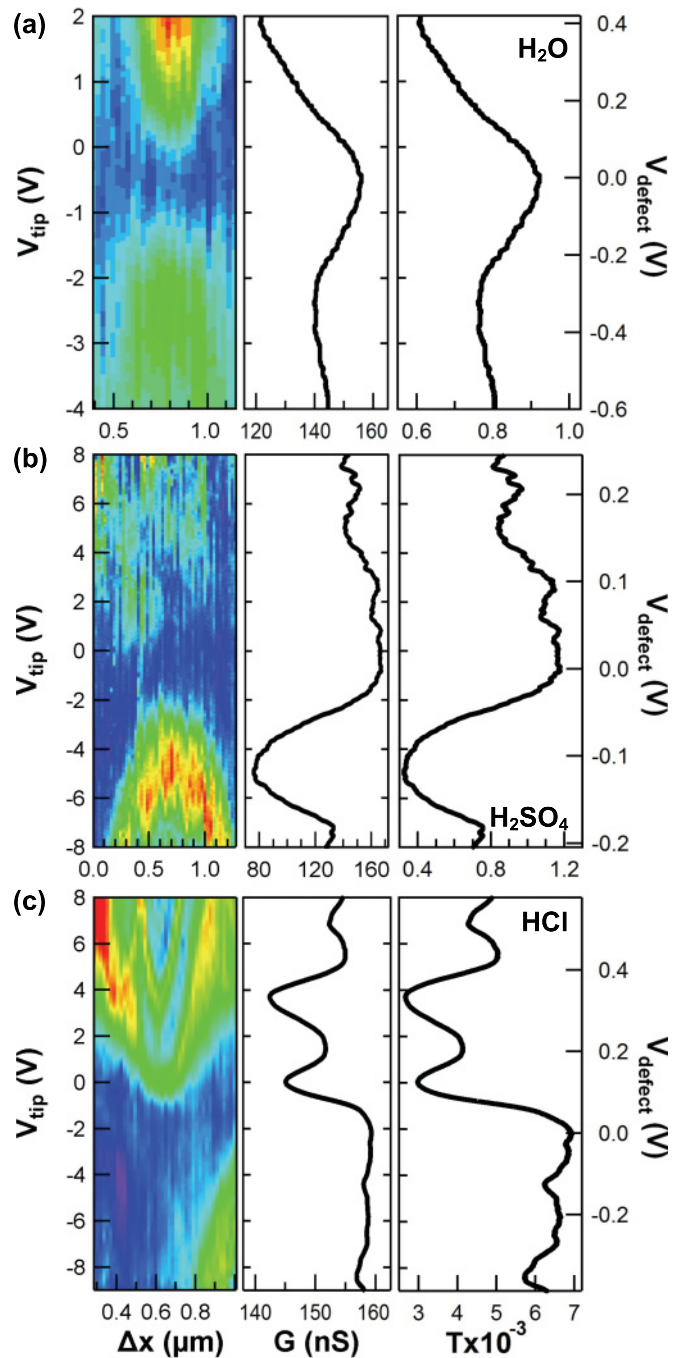

FIG. 3. (Color online) Characteristic data for s-SWNTs point functionalized in (a) H_2O, (b) H_2SO_4, and (c) HCl. Each depicts a portion of an SGS data set surrounding the defect site, the maximal $G(V_{\text{tip}})$ measured directly over the defect, and a transmission function $T(E)$ calculated from $G(V_{\text{tip}})$ and the contact resistance, as described in the text.

being nearly flat for $V_{\text{defect}} > 0$ and much steeper for $V_{\text{defect}} < 0$. The range of V_{tip} in Fig. 3(b) extends over a wider range than in Fig. 3(a), in order to resolve what is otherwise a very modest decline in $G(V_{\text{tip}})$ at positive bias. A second qualitative difference is a conspicuous ring of low G in the H_2SO_4 SGS image. This ring feature stands out particularly well because the $G(V_{\text{tip}})$ minimum is deep and bounded by maxima on both

sides. On the V_{defect} axis, the minimum occurs at -0.13 V and the second maximum is at -0.19 V.

Figure 3(c) continues the sequence with even more pronounced features. In this third example, a defect created by HCl oxidation again results in an asymmetric $G(V_{tip})$, with $G(V_{tip})$ nearly constant for all $V_{defect} < 0$. On the positive side of the V_{defect} axis, three oscillations of G maxima and minima are observed. The multiple maxima define a series of energies at which T_d is enhanced, suggesting multiple electronic states with an energy spacing of 0.2 eV. As a point of reference, 0.2 eV corresponds to the energy separation of SWNT carriers when confined within a 2 nm quantum dot,[7] suggesting a very reasonable length scale for the defect site.

The similarities in the $T_d(V_{defect})$ curves in Figs. 3(b) and 3(c) are striking if one accounts for the reversal in polarity. The curves share all of the same features, at least over the range where the experiments overlap. The values of $|V_{defect}|$ at the first minimum and second maximum are nearly equal in the two cases. Apparently, the bias range that has the least effect on an H_2SO_4 defect results in the largest oscillations on the HCl defect, and vice versa. Both examples involve m-SWNTs, so the difference is not simply due to n-type carriers versus p-type ones. Instead, we suspect that the defects may incorporate fixed charges due to electron affinities of the attached chemical groups, and that fixed charges having opposite signs could respond to the same V_{tip} bias with opposite polarities. Further evidence for defect charging is discussed in Sec. III D.

Additional, quantitative comparison of the three $T_d(V_{defect})$ curves can compare peak width, peak spacing, and the varying ranges of gate-independent G. The HCl oxidation resulted in narrow peaks suggestive of resonant tunneling through localized, molecule-like states. Interpreting such features will be the first step towards developing a “fingerprint” of the electronic effects of chemically distinct defects. However, further quantitative analysis or first principles modeling risks over interpretation of the current experimental results. Even though the qualitative differences highlighted in Fig. 3 have been established using measurements on multiple devices, the specific patterns of peaks and other unique features vary from sample to sample. Variation in the oxidation process, for example, can lead to overoxidation, spatially extended defects, and a broadening of $T_d(V_{defect})$ curves that is entirely independent of the electrolyte chemistry. The following two sections focus on this variability and also a bistability that complicates many experiments.

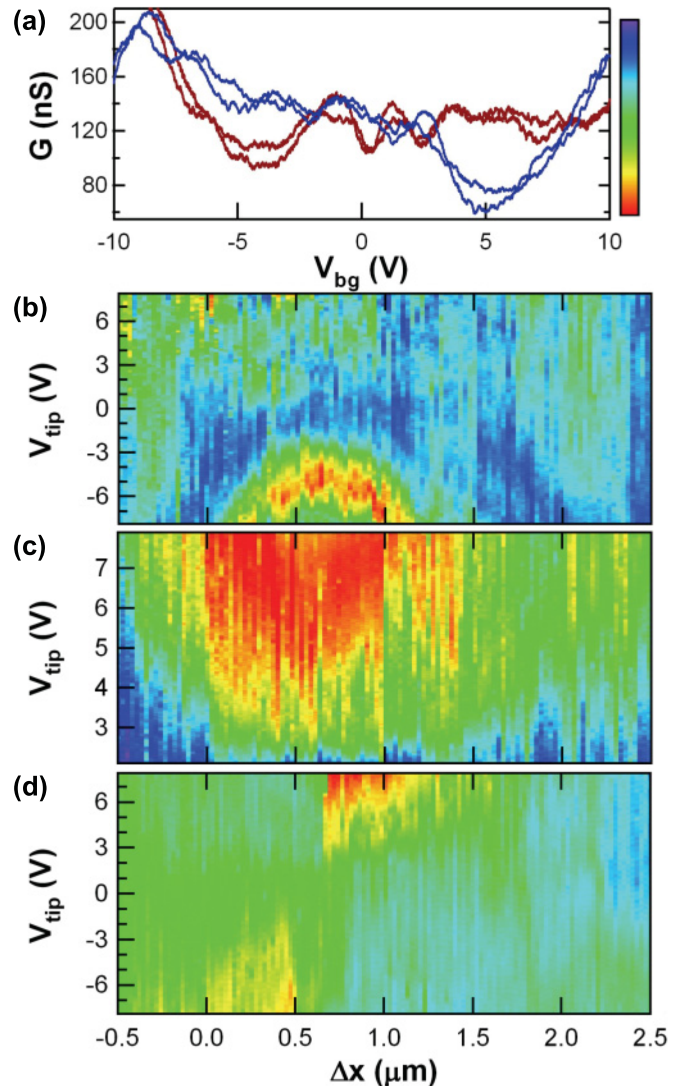

FIG. 4. (Color online) (a) A defect created in H_2SO_4 produces two similar but distinct $G(V_{bg})$ behaviors. For each state, two overlapping curves depict measurements at $V_{sd} = +100$ and -100 mV. (b) In the first state (red curve), the SGS image depicts scattering at $V_{tip} < 0$. (c) In the second state (blue curve), SGS imaging only occurs for $V_{tip} > 0$. (d) During some acquisitions, the device switches between its two states as the probe passes the defect site responsible for the response. A single color scale connects all three images to the $G(V_{bg})$ data.

D. Bistability of defect sites

Entirely separate from the features described above, another substantial difference occurs in the stability of the three types of defects studied. At room temperature, defects add conductance noise, and this contribution presumably reflects the defects' electronic or chemical internal degrees of freedom interacting with the SWNT current. Defect-induced noise is normally quenched upon cooling devices, but of course the internal degrees of freedom remain and can be excited by the scanning probe. This section describes bistability observed during SGS imaging that proves to depend on the electrolyte used during point functionalization.

Figure 4 illustrates bistability in the H_2SO_4-oxidized device discussed previously in Fig. 3(b). At 130 K, this m-SWNT exhibits two, readily distinguishable $G(V_{bg})$ characteristics shown in Fig. 4(a). In one state (red curve), G is relatively flat for $V_{bg} > 0$ and has a strong dip at $V_{bg} = -4$ V. The second state (blue) has nearly the opposite behavior, being flat except for a strong dip at $V_{bg} = 5$ V. For each state, two $G(V_{bg})$ curves are shown corresponding to positive and negative V_{sd}, indicating that the effect is not a simple nonlinearity. SGS can be performed in either of the two states, with the result that the same SWNT device produces two different SGS images. In the first state, a decrease in G is observed around a defect at $\Delta x = 0.6$ μm for $V_{tip} < -2$ V [see Fig. 4(b)]. In the second

state, a similar decrease is observed but for $V_{tip} > 2$ V [see Fig. 4(c)]. Good agreement of the SGS images with the $G(V_{bg})$ curves, and the concentration of the gate response around the defect site, are both consistent with the fact that the SWNT was semimetallic before point functionalization.

Testing has proven that the change from one state to the other is highly reversible and can be induced by the repeated passage of the tip over the defect site at certain V_{tip} values. For example, scanning the tip over the defect site at a bias $V_{tip} > 8$ V is likely to drive the device into the state depicted by Fig. 4(c). If the bias is reduced to $V_{tip} < 2$ V, then it can induce a switch to the state in Fig. 4(b). Switching is never caused by changes to V_{bg} or by remote tip motion far from the defect site, so we do not believe the effect is due to tip contamination or tip jumping.[59] The bistability is especially problematic for stable SGS imaging, since each image involves multiple ramps of V_{tip} directly over the defect site. Images can be reliably acquired using a limited bias range, but over larger ranges the tip directly perturbs the defect site during image acquisition. Fig. 4(d) shows an example of this, with the SWNT flipping from the first state to its second in the middle of the image, as the probe tip traverses the defect position.

These observations all suggest an electrostatic variability localized at the defect site. Charge injection could easily change the sign of a partially charged adduct (i.e., from $+0.5$ to -0.5e), but a field-induced rearrangement of the defect chemistry is also a possibility. Either way, the mirror symmetry in the $G(V_{bg})$ curves and SGS images suggests that the gating has opposite effects upon the two states. The energy level of a defect site alternately charged with $+q$ and $-q$ could certainly respond to gating in two opposite directions, but exactly how this charge modulates G remains unclear. Additional experiments, coupled with theoretical modeling, are necessary to establish a better understanding of the mechanism involved.

Despite uncertainty in the mechanism, experiments prove that this bistability is a useful way to discriminate among different types of defects. The behaviors described above are consistent attributes of H_2SO_4 defects and have been observed in more than 10 devices (though the manifestation is more difficult to observe in p-type s-SWNTs, than in m-SWNTs, because in the former $G(V_{bg})$ drops to zero for $V_{bg} > 0$ V). H_2O defects, on the other hand, exhibit a qualitatively different $G(V_{bg})$ bistability, and HCl defects exhibit almost none at all. Separate transport and noise measurements in the HCl case suggest that tip-charging effects still exist, but with relaxation pathways that are too fast to affect SGS imaging.

SWNT devices point functionalized in H_2O, and especially those with multiple defects, exhibit many of the same bistable characteristics as the H_2SO_4 case described above. However, the modest V_{bg} sensitivity of H_2SO_4 defects is replaced by much stronger gate dependence in the H_2O case. Figure 5(a) shows the two possible $G(V_{bg})$ characteristics for a m-SWNT device point functionalized in H_2O. In one state (red curve), G is predominantly p type, while in the second state (blue curve) it is n type. Note that G is plotted on a logarithmic scale.

Another difference between H_2SO_4 and H_2O defects is that the latter type switches much more predictably. At modest biases $|V_{tip}| > 3$ V, over 90% of tip traverses change the state of H_2O-oxidized SWNTs. Switching can also be induced

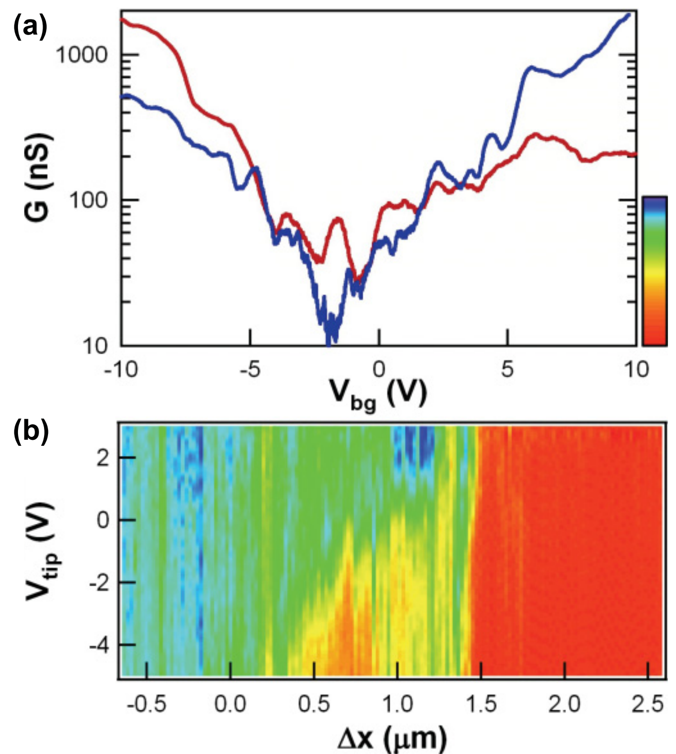

FIG. 5. (Color online) (a) A defect produced in H_2O results in two dissimilar $G(V_{bg})$ behaviors that are predominantly p or n type. (b) A single SGS image from the same device, capturing switching between the two states as the tip traverses the defect site. Defects produced in H_2O prove to be the most difficult to image, even when acquired using modest V_{tip} ranges.

by setting $|V_{bg}| > 5$ V. As a result of this sensitivity, SGS images like Fig. 3(a) are unusually difficult to obtain around H_2O defect sites. Fig. 5(b) is a more typical SGS image corresponding to the curves in Fig. 5(a). In this example, the device begins in its p-type state, but then transitions from the p-type state to the n-type state and back on every pass of the tip from $\Delta x = 1.4$ μm up to $\Delta x = 1.5$ μm. Because the switching occurs at progressively larger V_{tip} values on each pass, the transition in the SGS image appears slanted in the Δx- V_{tip} plane. The smoothness of the transition illustrates the reliability of the switching, and further suggests that the energetic barrier pinning the defect into one state or the other can be continuously varied by V_{tip}. Images having the opposite contrast can be obtained by setting $V_{bg} > 5$ V so that the device begins in the n-type state.

Even though the $G(V_{bg})$ behaviors in Figs. 4(a) and 5(a) are very different for the two electrolytes, both are consistent with the charge injection model proposed above. In the first case of H_2SO_4, the weak scattering means that charging the defect has only a modest effect. In the second case of H_2O, the same degree of charging has an effect amplified by the very deep minimum in $G(V_{bg})$. A positively-charged defect site blocks p-type carriers more strongly than n-type carriers, and a negatively-charged defect does the opposite. Thus, charge injection from the tip to the defective region gives the device a persistent memory that selects for one type of carrier over the other. The low-conductance feature at $V_{bg} = -2$ V in Fig. 5(a)

is intriguing because it is seven times more conductive in one state than the other, but further study is necessary to determine whether such features are common among different devices.

E. Variation in the degree of SWNT oxidation

Ideally, point functionalization is performed near the threshold of oxidation where individual, covalent events are stochastically separated in time. Under those conditions, sharp, discrete drops in $G(t)$ indicate the covalent addition of individual point defects. Reproducible point defects are prerequisite for the defect-to-defect comparison described above. However, two variations in the point functionalization process are common, and both result in more extensive oxidation and complexity that prevents reliable and reproducible analysis. This section discusses these variations and the SGS images that result.

First, consider the case of optimum point functionalization. In Fig. 6(a), point functionalization proceeds as desired, with a pair of sharp drops occurring within $\Delta t = 0.1$ s and leaving $G(t)$ in a low conductance state. Upon electrochemical reduction, devices returned nearly all the way to G_{pristine}. Defects incorporated in this manner were rarely evident in room temperature $G(V_{\text{bg}})$ measurements except at specific values of V_{bg}, justifying the discussion of high transparency in Sec. III B. These properties are also consistent with the premise of single defect incorporation, so they have been used as criteria for selecting images here and in previous reports.[15,26]

Figure 6(b) depicts a common example of point functionalization that does not proceed in the desired sequence. Electrochemical oxidation is not halted after the initial step or series of steps in $G(t)$ because the transitions do not decrease monotonically. Instead, bistable switching in $G(t)$ persists for one or more seconds. The metastable, rapidly switching intermediate levels are believed to reflect competition between covalent and noncovalent configurations of ions interacting with the SWNT sidewall,[33] and may also indicate the creation and spatial reorganization of multiple defects clustered together.[60] After oxidation along the lines of Fig. 6(b) and subsequent chemical reduction, SWNTs recover just 20–80% of G_{pristine}. Substantial new V_{bg} dependence is observed at room temperature, indicating T_d values comparable to the contact resistance. At lower temperatures, T_d becomes much less than 1% and adopts complex gate dependences. These properties result in SGS images that are not immediately distinguishable from those in Figs. 1–3, but which upon analysis have features that are unique to a particular device. An example is shown in the inset to Fig. 6(b). The greater complexity of these compound defects prevents reliable and reproducible analysis.

A third type of oxidation is also possible in which no discrete changes are observed at all. Fig. 6(c) depicts an example in which $G(t)$ decreases to zero continuously and smoothly over the course of 40 s. Devices that oxidize in this manner may not conduct at all after chemical reduction, and those which do only recover a small fraction of G_{pristine}. Both cases indicate a greater degree of oxidation, almost certainly extending over multiple sidewall sites. In fact, a similar type of spatially extended oxidation has been directly imaged by

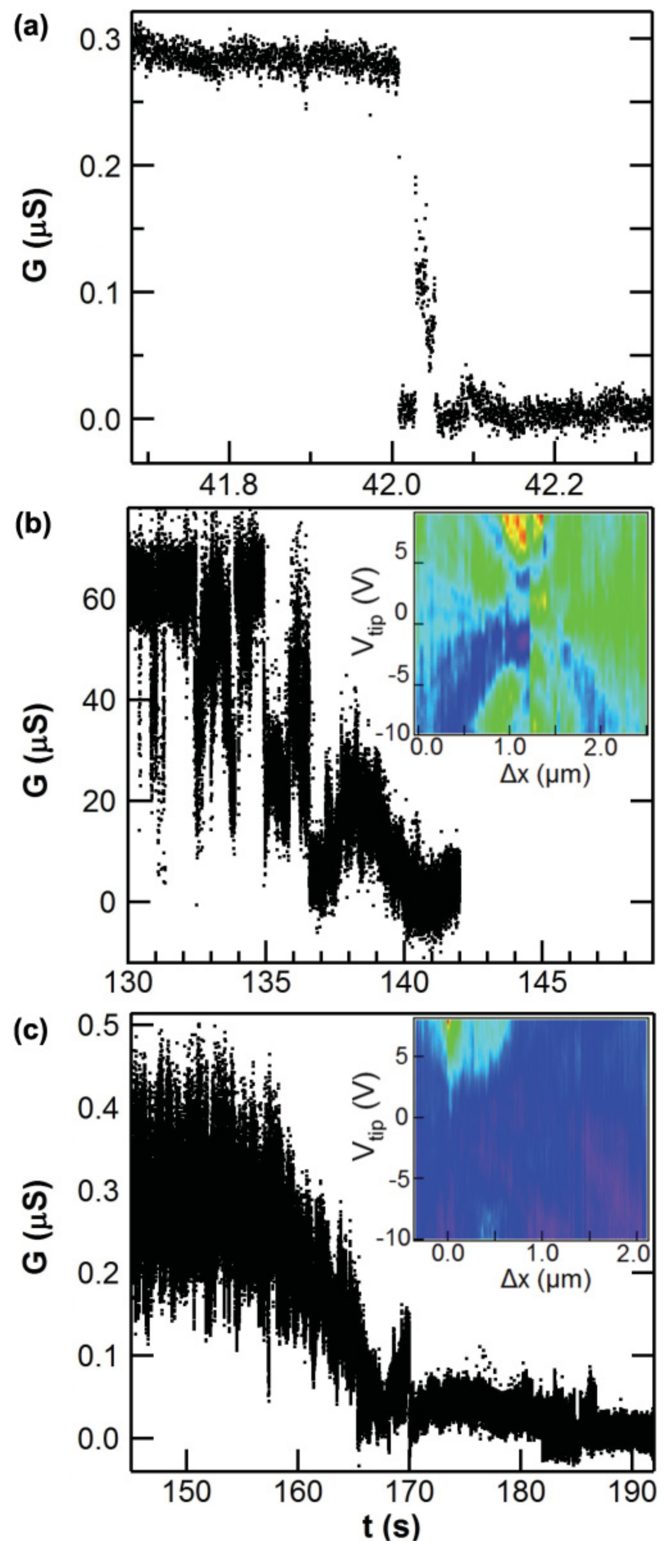

FIG. 6. Variability of point functionalization in HCl for three SWNT devices. (a) One or two discrete drops in conductance occurring in $\Delta t < 1$ s indicates the most likely creation of a covalent point defect. (b) Multiple drops with bistable dynamics over a few seconds suggests more complex damage, such as the creation and clustering of multiple sites. (c) A continuous decrease over many seconds indicates extensive and irreversible oxidation. In all three examples, individual data points correspond to 5 kHz sampling rate. Insets show example SGS images for the less ideal cases.

electron microscopy.[61] Of those devices which do conduct, SGS imaging usually reveals a relatively simple and one-sided $G(V_{tip})$ that is featureless at one polarity and exponentially and monotonically decreasing at the opposite polarity. An example SGS image is shown in the inset to Fig. 6(c). First-principles calculations have calculated the transmission of multiple clustered defects in different arrangements, but a multitude of possible arrangements limits any meaningful comparisons with experiment. Because the degree of experimental damage is impossible to verify in these cases, attention has instead focused on the simplest types of oxidation represented by Fig. 6(a).

All three types of $G(t)$ oxidation sequences are possible in SWNT devices, even using the same electrolyte. For instance, all three examples in Fig. 6 are obtained using HCl. In either HCl or H_2O, only 2 out of 10 device oxidations produced traces like the one shown in Fig. 6(a). This success rate, albeit limited, was sufficient to allow the comparative SGS analysis done in Fig. 3. The majority of the oxidations proceeded smoothly as in Fig. 6(c). Accordingly, the original report on point functionalization identified H_2O, HCl, and NaOH as the poorest candidates for successful point functionalization because of their unreliable production of discrete oxidation and/or reduction steps in $G(t)$.[15] On the other hand, $G(t)$ traces like Figs. 6(a) or 6(b) occur with a 90% probability when point functionalization is performed in H_2SO_4 or HNO_3. This high success rate makes the production of point defects relatively straightforward in these acids. Nevertheless, the remaining possibility of a nonideal oxidation as in Fig. 6(b), combined with the metastable switching described in Sec. III D, conspire to make SGS imaging time consuming and difficult to analyze even in this case.

IV. CONCLUSION

To summarize, successful point functionalization introduced scattering sites that were quantitatively probed by the SGS technique. Functionalization in three different electrolytes resulted in defect sites exhibiting clearly distinguishable characteristics. All three types of defects responded to gating with a dominant transmission maximum, but the conductance on either side of this peak was electrolyte dependent. Oxidation in H_2O produced the most symmetric response, with G substantially reduced on either side of the transmission peak. H_2SO_4 and HCl oxidations both produced more asymmetric characteristics that were substantially transparent at one polarity and contained one or more transmission minima at the other polarity. H_2SO_4 oxidation produced a single transmission minimum that resulted in distinctive SGS images. HCl oxidation, on the other hand, produced a series of multiple, shallower minima.

The stability and reproducibility of a given SGS image was also found to be dependent on the electrolyte used. H_2O defects reliably switched between two states having dissimilar conductances. H_2SO_4 defects also exhibited two distinct states, but they were less different in conductance and metastable or longer-lived in the presence of a biased tip. HCl defects had a very transient bistability that was difficult to characterize, but which resulted in the most stable imaging conditions of the three.

In all three electrolytes, the observed transmission curves were interpreted in terms of differences in the underlying electronic structure of defect state, but the analysis in this direction remains preliminary. The experimental data provide the impetus for further measurements, to be combined with first principles modeling of these effects.

ACKNOWLEDGMENTS

This work was sponsored by the NSF under grants DMR-0801271, DMR-1104629, and ECS-0802077. BLC performed all device fabrication with support from Nanostructures for Electrical Energy Storage, an Energy Frontier Research Center funded by the US Department of Energy, Office of Science, Office of Basic Energy Sciences under Award Number DESC0001160.

*Corresponding author: collinsp@uci.edu

[1] H. G. Grimmeiss and M. Kleverman, Adv. Mater. **4**, 261 (1992).

[2] L. Dobaczewski, A. R. Peaker, and K. B. Nielsen, J. App. Phys. **96**, 4689 (2004).

[3] M. J. Kirton and M. J. Uren, Adv. Phys. **38**, 367 (1989).

[4] P. M. Koenraad and M. E. Flatte, Nat. Mater. **10**, 91 (2011).

[5] M. Fuechsle, J. A. Miwa, S. Mahapatra, H. Ryu, S. Lee, O. Warschkow, L. C. L. Hollenberg, G. Klimeck, and M. Y. Simmons, Nat. Nano. **7**, 242 (2012).

[6] M. S. Purewal, B. H. Hong, A. Ravi, B. Chandra, J. Hone, and P. Kim, Phys. Rev. Lett. **98**, 186808 (2007).

[7] M. J. Biercuk, S. Ilani, C. M. Marcus, and P. L. McEuen, in *Carbon Nanotubes*, edited by A. Jorio, G. Dresselhaus, and M. S. Dresselhaus (Springer-Verlag, Berlin, 2008), Vol. 111, p. 455.

[8] W. J. Liang, M. Bockrath, and H. Park, Ann. Rev. Phys. Chem. **56**, 475 (2005).

[9] P. G. Collins, in *Oxford Handbook of Nanoscience and Technology: Frontiers and Advances*, edited by A. V. Narlikar and Y. Y. Fu (Oxford University Press, Oxford, 2010).

[10] S. Banerjee, T. Hemraj-Benny, and S. S. Wong, Adv. Mater. **17**, 17 (2005).

[11] P. Singh, S. Campidelli, S. Giordani, D. Bonifazi, A. Bianco, and M. Prato, Chem. Soc. Rev. **38**, 2214 (2009).

[12] A. Hartschuh, E. J. Sanchez, X. S. Xie, and L. Novotny, Phys. Rev. Lett. **90**, 095503 (2003).

[13] N. Anderson, A. Hartschuh, and L. Novotny, Nano. Lett. **7**, 577 (2007).

[14] J. J. Crochet, J. G. Duque, J. H. Werner, and S. K. Doorn, Nat. Nano. **7**, 126 (2012).

[15] B. R. Goldsmith, J. G. Coroneus, V. R. Khalap, A. A. Kane, G. A. Weiss, and P. G. Collins, Science **315**, 77 (2007).

[16] S. G. Louie, *Carbon Nanotubes* (Springer-Verlag, Berlin, 2001), Vol. 80, p. 113.

[17]*Scanning Probe Microscopy : Electrical and Electromechanical Phenomena at the Nanoscale*, edited by S. V. Kalinin and A. Gruverman (Springer, New York, 2007).
[18]M. Bockrath, W. J. Liang, D. Bozovic, J. H. Hafner, C. M. Lieber, M. Tinkham, and H. Park, Science **291**, 283 (2001).
[19]M. Freitag, A. T. Johnson, S. V. Kalinin, and D. A. Bonnell, Phys. Rev. Lett. **89**, 216801 (2002).
[20]S. V. Kalinin, D. A. Bonnell, M. Freitag, and A. T. Johnson, App. Phys. Lett. **81**, 5219 (2002).
[21]Y. Kim, Y. M. Oh, J. Y. Park, and S. J. Kahng, Nanotechnology **18**, 475712 (2007).
[22]J. S. Lee, S. Ryu, K. Yoo, J. Kim, I. S. Choi, and W. S. Yun, Ultramicroscopy **108**, 1045 (2008).
[23]N. Aoki, K. Sudou, K. Matsusaki, and Y. Ochiai, J. Vac. Sci. Technol. B **27**, 785 (2009).
[24]M. Huefner, C. May, S. Kicin, K. Ensslin, T. Ihn, M. Hilke, K. Suter, N. F. de Rooij, and U. Staufer, Phys. Rev. B **79**, 134530 (2009).
[25]M. G. Pala, S. Baltazar, F. Martins, B. Hackens, H. Sellier, T. Ouisse, V. Bayot, and S. Huant, Nanotechnology **20**, 264021 (2009).
[26]S. R. Hunt, D. Wan, V. R. Khalap, B. L. Corso, and P. G. Collins, Nano. Lett. **11**, 1055 (2011).
[27]A. Müller, S. K. Das, P. Kogerler, H. Bogge, M. Schmidtmann, A. X. Trautwein, V. Schunemann, E. Krickemeyer, and W. Preetz, Angew. Chem., Int. Ed. **39**, 3414 (2000).
[28]L. An, J. M. Owens, L. E. McNeil, and J. Liu, J. Am. Chem. Soc. **124**, 13688 (2002).
[29]S. M. Huang, B. Maynor, X. Y. Cai, and J. Liu, Adv. Mater. **15**, 1651 (2003).
[30]J. W. Mintmire, B. I. Dunlap, and C. T. White, Phys. Rev. Lett. **68**, 631 (1992).
[31]N. Hamada, S. I. Sawada, and A. Oshiyama, Phys. Rev. Lett. **68**, 1579 (1992).
[32]J. G. Coroneus, B. R. Goldsmith, J. A. Lamboy, A. A. Kane, P. G. Collins, and G. A. Weiss, Chem. Phys. Chem. **9**, 1053 (2008).
[33]Y. Kanai, V. R. Khalap, P. G. Collins, and J. C. Grossman, Phys. Rev. Lett. **104**, 066401 (2010).
[34]Y. Fan, B. R. Goldsmith, and P. G. Collins, Nat. Mater. **4**, 906 (2005).
[35]A. Bachtold, M. S. Fuhrer, S. Plyasunov, M. Forero, E. H. Anderson, A. Zettl, and P. L. McEuen, Phys. Rev. Lett. **84**, 6082 (2000).
[36]M. Freitag, M. Radosavljevic, Y. X. Zhou, A. T. Johnson, and W. F. Smith, App. Phys. Lett. **79**, 3326 (2001).
[37]S. Heinze, J. Tersoff, R. Martel, V. Derycke, J. Appenzeller, and P. Avouris, Phys. Rev. Lett. **89**, 106801 (2002).
[38]J. Svensson, A. A. Sourab, Y. Tarakanov, D. S. Lee, S. J. Park, S. J. Baek, Y. W. Park, and E. E. B. Campbell, Nanotechnology **20**, 5 (2009).
[39]C. Staii, A. T. Johnson, R. Shao, and D. A. Bonnell, Nano. Lett. **5**, 893 (2005).
[40]J. Appenzeller, J. Knoch, V. Derycke, R. Martel, S. Wind, and P. Avouris, Phys. Rev. Lett. **89**, 126801 (2002).
[41]W. Kim, A. Javey, R. Tu, J. Cao, Q. Wang, and H. Dai, Appl. Phys. Lett. **87**, 173101 (2005).
[42]Z. Chen, J. Appenzeller, J. Knoch, Y. Lim, and P. Avouris, Nano. Lett. **5**, 1497 (2005).
[43]S. J. Tans and C. Dekker, Nature (London) **404**, 834 (2000).
[44]M. T. Woodside and P. L. McEuen, Science **296**, 1098 (2002).
[45]S. Ilani, L. A. K. Donev, M. Kindermann, and P. L. McEuen, Nat. Phys. **2**, 687 (2006).
[46]X. J. Zhou, J. Y. Park, S. M. Huang, J. Liu, and P. L. McEuen, Phys. Rev. Lett. **95**, 146805 (2005).
[47]J. Mannik, B. R. Goldsmith, A. Kane, and P. G. Collins, Phys. Rev. Lett. **97**, 016601 (2006).
[48]D. J. Perello, Y. Woo Jong, B. Dong Jae, C. Seung Jin, M. J. Kim, L. Young Hee, and Y. Minhee, J. App. Phys. **105**, 124309 (2009).
[49]X. Lu and Z. F. Chen, Chem. Rev. **105**, 3643 (2005).
[50]J. Zhao, Z. F. Chen, Z. Zhou, H. Park, P. V. Schleyer, and J. P. Lu, ChemPhysChem **6**, 598 (2005).
[51]Y. W. Son, J. Ihm, M. L. Cohen, S. G. Louie, and H. J. Choi, Phys. Rev. Lett. **95**, 216602 (2005).
[52]Y. S. Lee, M. B. Nardelli, and N. Marzari, Phys. Rev. Lett. **95**, 076804 (2005).
[53]J. Ihm, J.-H. Eom, H. Lee, J. Im, C. Park, B. W. Jeong, and S. Kim, Physica B **376–377**, 7 (2006).
[54]Y.-S. Lee and N. Marzari, Phys. Rev. Lett. **97**, 116801 (2006).
[55]L. M. Zhang and M. M. Fogler, Nano. Lett. **6**, 2206 (2006).
[56]D. Sarid, *Exploring Scanning Probe Microscopy with* MATHEMATICA (Wiley-VCH, New York, 2007).
[57]For simplicity, we neglect the fourfold degeneracy and use a single transmission coefficient *Td* rather than a four-by-four transmission matrix.
[58]S. Datta, *Electronic Transport in Mesoscopic Systems* (Cambridge University Press, Cambridge, 1995).
[59]M. Rozler and M. R. Beasley, Rev. Sci. Instrum. **79**, 073904 (2008).
[60]M. K. Ashraf, N. A. Bruque, R. R. Pandey, P. G. Collins, and R. K. Lake, Phys. Rev. B **79**, 115428 (2009).
[61]Y. Zhang and Y. Wang, J. Phys. Chem. Lett. **2**, 885 (2011).